The Astrophysical Journal, 777:16 (9pp), 2013 November 1 doi:10.1088/0004-637X/777/1/16

NUMERICAL SIMULATIONS OF CHROMOSPHERIC ANEMONE JETS ASSOCIATED WITH MOVING MAGNETIC FEATURES

Liping Yang[1,2], Jiansen He[1], Hardi Peter[3], Chuanyi Tu[1], Lei Zhang[1], Xueshang Feng[2], and Shaohua Zhang[4]
[1] School of Earth and Space Sciences, Peking University, 100871 Beijing, China; jshept@gmail.com
[2] SIGMA Weather Group, State Key Laboratory for Space Weather, Center for Space Science and Applied Research, Chinese Academy of Sciences, 100871 Beijing, China
[3] Max Planck Institute for Solar System Research, D-37191 Katlenburg-Lindau, Germany
[4] Institute of Geology and Geophysics, Chinese Academy of Sciences, 100871 Beijing, China
Received 2013 March 29; accepted 2013 July 30; published 2013 October 9

ABSTRACT

Observations with the space-based solar observatory *Hinode* show that small-scale magnetic structures in the photosphere are found to be associated with a particular class of jets of plasma in the chromosphere called anemone jets. The goal of our study is to conduct a numerical experiment of such chromospheric anemone jets related to the moving magnetic features (MMFs). We construct a 2.5 dimensional numerical MHD model to describe the process of magnetic reconnection between the MMFs and the pre-existing ambient magnetic field, which is driven by the horizontal motion of the magnetic structure in the photosphere. We include thermal conduction parallel to the magnetic field and optically thin radiative losses in the corona to account for a self-consistent description of the evaporation process during the heating of the plasma due to the reconnection process. The motion of the MMFs leads to the expected jet and our numerical results can reproduce many observed characteristics of chromospheric anemone jets, topologically and quantitatively. As a result of the tearing instability, plasmoids are generated in the reconnection process that are consistent with the observed bright moving blobs in the anemone jets. An increase in the thermal pressure at the base of the jet is also driven by the reconnection, which induces a train of slow-mode shocks propagating upward. These shocks are a secondary effect, and only modulate the outflow of the anemone jet. The jet itself is driven by the energy input due to the reconnection of the MMFs and the ambient magnetic field.

Key words: magnetic reconnection – shock waves – Sun: chromosphere

Online-only material: color figures

1. INTRODUCTION

Recent solar space missions such as the *Solar Dynamics Observatory*, *Hinode*, *Yohkoh*, the *Solar and Heliospheric Observatory*, and the *Transition Region and Coronal Explorer* have showed that the lower solar atmosphere is much more dynamic than what had been expected. The lower solar atmosphere is filled with numerous fine structures such as spicules, surges, Ellerman bombs, chromospheric anemone jets, mottles, fibrils, etc., as observed at various wavelengths and in various regions (Shibata et al. 2007; Katsukawa et al. 2007; Cirtain et al. 2007). Discovered by the Solar Optical Telescope onboard *Hinode*, chromospheric anemone jets are observed to be much smaller and much more frequent than surges (Shibata et al. 2007). The footpoints of these jets usually display bright cusp or inverted Y-shaped structures and do not look like simple bright points. These jets are often accordingly referred to morphologically as "chromospheric anemone jets." A statistical study performed by Nishizuka et al. (2011) showed that the chromospheric anemone jets have typical lengths of 1.0–4.0 Mm, widths of 100–400 km, and cusp sizes of 700–2000 km. Their lifetime is about 100–500 s and their velocity is about 5–20 km s^{-1}. Simultaneous magnetic field observations show that such jet events are favorably located in mixed-polarity regions or near the boundary between opposite polarities, which are associated with either small emerging flux regions or moving magnetic features (MMFs; Morita et al. 2010, 2012).

Running difference images of chromospheric anemone jets exhibit multiple bright plasma blobs in their footpoint, which also appear as multiple brightnesses in the light curve of the footpoint of the jets (Singh et al. 2011, 2012). These bright blobs are formed in one leg of the cusp at the bottom of the inverted Y-shaped jet and appear recurrently at the same location. After their formation, these blobs are ejected bi-directionally along the leg, with ejections toward the jet being more common. The typical velocity of the upward plasma blobs is about 30 km s^{-1}. The upwardly moving blobs collide with the jets soon after their formation, lose their blob-like shapes, and launch jet-like impulses.

On the basis of the observations, chromospheric anemone jets are suspected to be the result of magnetic reconnection (Shibata et al. 2007; Katsukawa et al. 2007; Nishizuka et al. 2008; Morita et al. 2010; Singh et al. 2011, 2012; Nishizuka et al. 2011; Morita et al. 2012). Once an emerging bipole or a moving bipole collides with ambient fields, reconnection is expected to occur. When a bipole connects to polar opposite ambient field, bright cusp or inverted Y-shaped structures will be generated and the heated plasma will be expelled, forming the jets. Most of the footpoints of chromospheric anemone jets lie in mixed-polarity regions, providing indirect evidence of magnetic reconnection. Also, the apparent velocity of the jet is close to the local Alfvén speed, which is consistent with the reconnection model. Furthermore, the multiple plasma ejections from the footpoints of the jets indicate that the formation process of chromospheric anemone jets occurs quite rapidly and intermittently, which is consistent with features of plasmoids induced by reconnections due to the resistive tearing mode instability.

Since the observation of Ca II H brightening near the disk center shows that chromospheric anemone jets are often associated with small-scale flux emergence events (Shibata et al. 2007; Nishizuka et al. 2008; Guglielmino et al. 2008; Morita et al. 2010, 2012), it is suggested that the jets are formed as a result of the interaction between the emerging magnetic flux and the pre-existing ambient fields in a manner similar to that of an anemone jet observed in soft X-rays. The differences between them mainly lie in the amount of the emerging flux. While coronal X-ray jets are related to the large-scale emerging flux and its reconnection with ambient fields at coronal heights (Shibata et al. 1992; Yokoyama & Shibata 1995, 1996; Shimojo et al. 1998), the chromospheric anemone jets are associated with the small-scale emerging flux and its reconnection in the chromospheric layer (Isobe et al. 2008; Guglielmino et al. 2008; Martínez-Sykora et al. 2009). Two-dimensional (2D) magnetohydrodynamics (MHD) simulations of the reconnection between emerging flux and uniform coronal fields have been conducted and they successfully reproduce both observed X-ray jets and Hα surges (Yokoyama & Shibata 1995, 1996). Nishizuka et al. (2008) and also the giant chromospheric anemone jets on the basis of the reconnection between emerging the flux and the pre-existing ambient field occurring in the transition region or upper chromosphere, producing high-speed jets of both hot and cool materials.

However, chromospheric anemone jets related to MMFs have not been studied intensively so far. MMFs are observed as small-scale magnetic features, initially appearing near the outer edge of sunspots and subsequently moving approximately radially outward from sunspots at about 1–2 km s^{-1} (Sheeley 1969; Harvey & Harvey 1973; Zhang et al. 1992). After having traveled about 10 Mm, MMFs coalesce with the surrounding photospheric network or disappear due to collisions with the ambient field with an opposite polarity (Hagenaar & Shine 2005). MMFs tend to appear in opposite polarity pairs and their typical diameters are about 1 Mm (Sheeley 1969; Hagenaar & Shine 2005). MMFs produce a very faint Hα signal and the direction of their motion is aligned with the direction of the Hα fibrils, which suggests that MMFs are low-lying loops (Ravindra 2006). By studying the properties and motions of Ellerman bombs around a sunspot in a mature active region (AR), Ravindra (2006) found that 36% of Ellerman bombs that they observed were associated with MMFs and that Ellerman bombs tracked MMFs well. Brooks et al. (2007) conducted a detailed study of Hα surges from cotemporal, high-resolution multiwavelength images of NOAA AR 8227 and found that the collisions between MMFs and emerging fields produce the observed surges.

In this paper, we conduct a numerical simulation of chromospheric anemone jets as driven by reconnection between MMFs and pre-existing ambient fields. For this purpose, a 2.5 dimensional (2.5D) MHD model with a domain extending from the lower chromosphere to the lower corona is used and a realistic energy equation is considered, which, in particular, includes thermal conduction, radiation losses, and heating. Here, we present the numerical results in which many observed features of chromospheric anemone jets are reproduced. The paper is organized as follows. In Section 2, a general description of the numerical MHD model, including basic equations, the numerical method, as well as the initial and boundary conditions, is presented. Section 3 presents the results of the numerical simulations and the analysis of them. Section 4 is reserved for a summary and discussion.

2. NUMERICAL MHD MODEL

The details of the numerical MHD model used here have been described in Yang et al. (2013). In this section, only the model's features and modifications specific to this study are given. The basic equations are 2.5D resistive MHD equations in Cartesian coordinates (x, y, z) with y directed vertically, which can be written as the following nondimensional form:

$$\frac{\partial \rho}{\partial t} + \nabla \cdot \rho \mathbf{u} = 0 \qquad (1)$$

$$\frac{\partial \rho \mathbf{u}}{\partial t} + \nabla \cdot \left[\rho \mathbf{u}\mathbf{u} + \mathbf{I}\left(p + \frac{1}{2}\mathbf{B}^2\right) - \mathbf{B}\mathbf{B}\right] = \rho \mathbf{g} \qquad (2)$$

$$\begin{aligned} \frac{\partial e}{\partial t} &+ \nabla \cdot \left[\mathbf{u}\left(e + p + \frac{1}{2}\mathbf{B}^2\right) - (\mathbf{u}\cdot\mathbf{B})\mathbf{B}\right] \\ &= \rho \mathbf{u}\cdot\mathbf{g} + \nabla\cdot(\mathbf{B}\times\eta\mathbf{j}) - L_r + \nabla\cdot\mathbf{q} + H + C_N \qquad (3) \end{aligned}$$

$$\frac{\partial \mathbf{B}}{\partial t} + \nabla \cdot (\mathbf{u}\mathbf{B} - \mathbf{B}\mathbf{u}) = \eta \nabla^2 \mathbf{B}, \qquad (4)$$

where

$$e = \frac{1}{2}\rho \mathbf{u}^2 + \frac{p}{\gamma - 1} + \frac{1}{2}\mathbf{B}^2, \quad \mathbf{j} = \nabla \times \mathbf{B} \qquad (5)$$

corresponding to the total energy density and current density, respectively. Here, ρ is the mass density, $\mathbf{u} = (v_x, v_y, v_z)$ are the velocities in the x, y, and z directions, p is the thermal pressure, $\mathbf{B}$ denotes the magnetic field, t is time, $\mathbf{g}$ $(= -g\mathbf{e}_y$, $g = \text{const})$ is the solar gravitational acceleration, γ $(= 5/3)$ is the adiabatic index, and η is the magnetic resistivity. Since the solar chromosphere is fully collisional, anomalous resistivity as a result of various collisionless processes could not arise (Singh et al. 2011). Here, η is set to be uniform, with the magnetic Reynolds number (Rm) being about 2×10^6.

In the energy equation (Equation (3)), L_r describes radiative losses, which are treated in the optically thin limit using the cooling function described in Cook et al. (1989). $\nabla \cdot \mathbf{q}$ is the anisotropic thermal conduction, which plays an important role in the energy balance of the corona. The heat flux vector $\mathbf{q}$ is

$$\mathbf{q} = K_{\|}(\hat{b} \cdot \nabla T)\hat{b}, \qquad (6)$$

where T is the temperature, $\hat{b}$ is the unit vector of the magnetic field, and conduction across the magnetic field is inhibited as $K_{\perp} \ll K_{\|}$ in the solar atmosphere. Also, $K_{\|}$ is set to be temperature dependent (Abbett 2007; Yang et al. 2013) and has the following form. When $T > T_c$ $(T_c \equiv 3 \times 10^5\ \text{K})$, $K_{\|} = k_0 T^{5/2}$; elsewhere, $K_{\|} = k_0 T_c^{5/2}(1 + \tanh(4(T - T_{\text{ch}})/T_{\text{ch}}))/2 + k_0 T^{5/2}(1 - \tanh(4(T - T_{\text{ch}})/T_{\text{ch}}))/2$ $(T_{\text{ch}} \equiv 1 \times 10^4\ \text{K})$, where $k_0 = 1 \times 10^6$ in cgs units. This setup avoids a temperature gradient that becomes exceedingly steep, resulting in a transition region only a few km thick, similar to the treatment of Abbett (2007). To represent the effects of optically thick radiative cooling in the photosphere and low chromosphere, a Newton cooling term C_N is applied to the lower-most part of the model. It has the form given by Yang et al. (2013) and has little influence on the temperature distribution at heights above 0.2 Mm, where the radiative cooling is mainly due to optically thin emission.

In Equation (3), H is the heating term, which maintains the background corona against conductive, radiative, and solar wind losses. Since the physical mechanism of the heating origin is presently not known, H is designed to vary with the height y as

$$H_{\text{exp}} = \begin{cases} \frac{F}{\lambda}, & y \leqslant y_{\text{chr}} \\ \frac{F}{\lambda}\exp(-(y - y_{\text{chr}})/\lambda), & y > y_{\text{chr}}, \end{cases} \qquad (7)$$

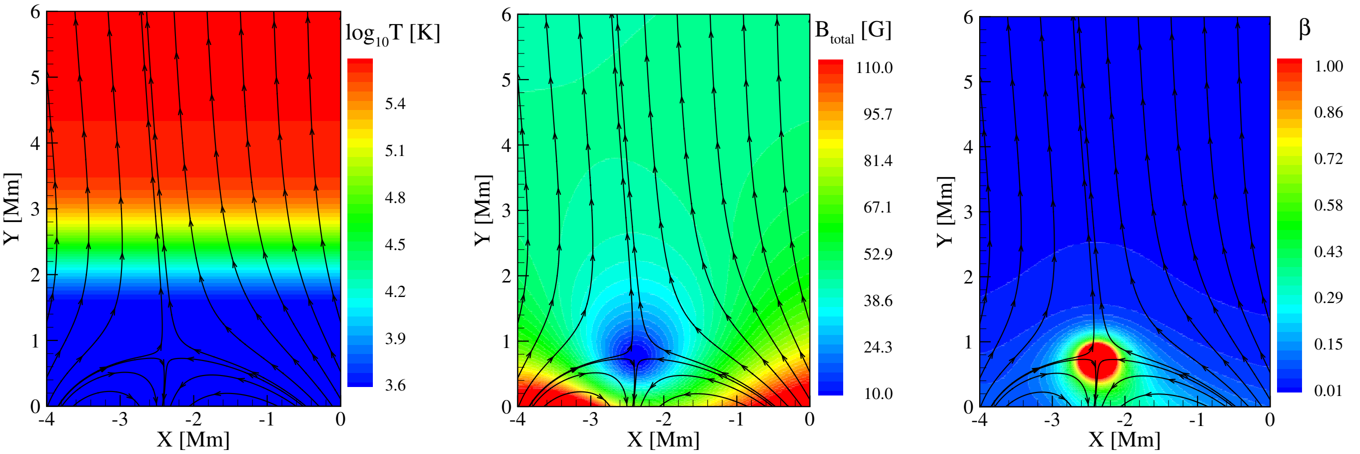

Figure 1. Initial distributions of temperature T, magnetic field strength B_{total}, and the plasma β. Magnetic field lines are shown in black.
(A color version of this figure is available in the online journal.)

where the energy flux F is 400 W m^{-2}, the damping length scale λ is 2 Mm, and y_{chr} is set to be 3 Mm. This form of the heating function has been employed frequently in 1D and 2D simulations (e.g., Hansteen & Leer 1995; Aiouaz et al. 2005).

In the simulation, three independent parameters, a reference density ρ_0 (5×10^{-4} kg m^{-3}), a reference temperature T_0 (5×10^3 K), and a typical length scale L_0 (1 Mm), are chosen to normalize the MHD equations. Other variables are normalized by their combinations. Accordingly, velocity, time scale, magnetic field, plasma pressure, current density, and resistivity are normalized by $V_0 = \sqrt{RT_0}$, $\tau_0 = L_0/V_0$, $B_0 = \sqrt{\mu\rho_0 V_0^2}$, $P_0 = B_0^2/\mu$, $J_0 = B_0/(\mu L_0)$, and $\eta_0 = \mu L_0 V_0$, respectively. Here, R is a gas constant and μ is the magnetic permeability of free space.

The simulation region is defined by -4 Mm $\leqslant x \leqslant 0$ Mm in the horizontal dimension and 0 Mm $\leqslant y \leqslant 6$ Mm in the vertical dimension. Initially, the domain is covered by uniform grid points both in the x and y dimensions with $\delta x = \delta y = 20$ km. During the computation, the smallest grid cells are set in the region with the strongest current, with $\delta x = \delta y = 1.25$ km as a result of the adaptive mesh refinement (AMR) used in the numerical model (Feng et al. 2011; Zhang et al. 2011). Our numerical scheme is a splitting-based, finite-volume scheme. The fluid part is solved by the second-order Godunov-type central scheme and the magnetic part by the constrained transport approach (Ziegler 2004). The explicit second-order total variation diminishing Runge–Kutta time stepping is applied in the time integration. We have tested the results with a larger grid size (1.5 times the present one), but the results, especially for the temperature and outflow in the reconnecting region, differ only in unessential aspects—the differences (e.g., $(T_{\text{coarse}} - T_{\text{fine}})/T_{\text{fine}}$) are less than 10%, which suggests that the presented results converge.

For the initial conditions, the gas is in hydrostatic equilibrium with a temperature prescribed by a hyperbolic tangent function. The initial distributions of the pressure and the density are derived by analytically solving the 1D static equation and ideal gas equation. The temperature and density in the photosphere are 5000 K and 5×10^{-4} kg m^{-3}, respectively. The initial velocity is set to zero. The initial magnetic field is a potential field, consisting of two parts, with one part given by Hackenberg et al. (2000) and the other generated by an infinite straight-line current flowing along the line at $x = -3.5$ Mm, $y = -0.7$ Mm. Figure 1 illustrates the initial distributions of temperature T, the magnetic field strength B_{total}, the plasma β ($\beta \equiv 2p/B_{\text{total}}$), and the constructed magnetic configuration.

Boundary conditions are as follows. Along the side boundaries at $x = 0$ Mm and $x = -4$ Mm, we use open conditions, i.e., there we set the normal gradients of ρ, $\mathbf{u}$, and T to zero and extrapolate $\mathbf{B}$ linearly. To ensure that upward propagating waves leave the computational domain without generating spurious reflections at the upper boundary at $y = 5$ Mm, free boundary conditions are implemented with virtual mesh points introduced as in Yokoyama & Shibata (1996). At the lower boundary of $y = 0$, the density ρ and temperature T are fixed. The tangential component v_x of the velocity is prescribed as $v_x = 1.5(1.0 - \exp(-|0.5x|))$ km s^{-1} to describe the motion of MMFs. The normal velocity component v_y is obtained by linear extrapolation. The values of the tangential components of the magnetic field (B_x, B_z) are given by setting the second normal derivative to zero, and $\nabla \cdot \mathbf{B} = 0$ is used to determine the normal component of the magnetic field (B_y).

3. NUMERICAL RESULTS

3.1. Dynamics in the Reconnection Region

After the initial system, as shown in Figure 1, is relaxed into a quasi-steady state, the horizontal flow is introduced to describe the movement of MMFs due to the presence of radiative losses, thermal conduction, and heating. Figure 2 shows the calculated distributions of number density N and temperature T at $t = 1.0$ minute, $t = 2.8$ minutes, and $t = 4.3$ minutes. In this figure, streamlines in the top row denote magnetic field lines and black arrows and white lines in the bottom row indicate velocity and the values of β, respectively.

From Figure 2, we can see that the MMFs, transported by the horizontal flow, migrate toward the pre-existing ambient field region. As a result, their interface deforms to generate a current sheet around the magnetic null point. When the current density strengthens significantly, reconnection between MMFs and pre-existing ambient fields takes place, producing both upward and downward heated outflows. At $t = 1.0$ minute, the collision between the MMFs and the ambient fields creates a thin current sheet at the interface, initiating the reconnection. Meanwhile, the plasma on both sides of the current sheet is pushed into the diffusion region. The plasma in the diffusion region is heated by Joule heating rather than the parameterized heating H, which is mostly balanced by conductive, radiative, and mass losses.

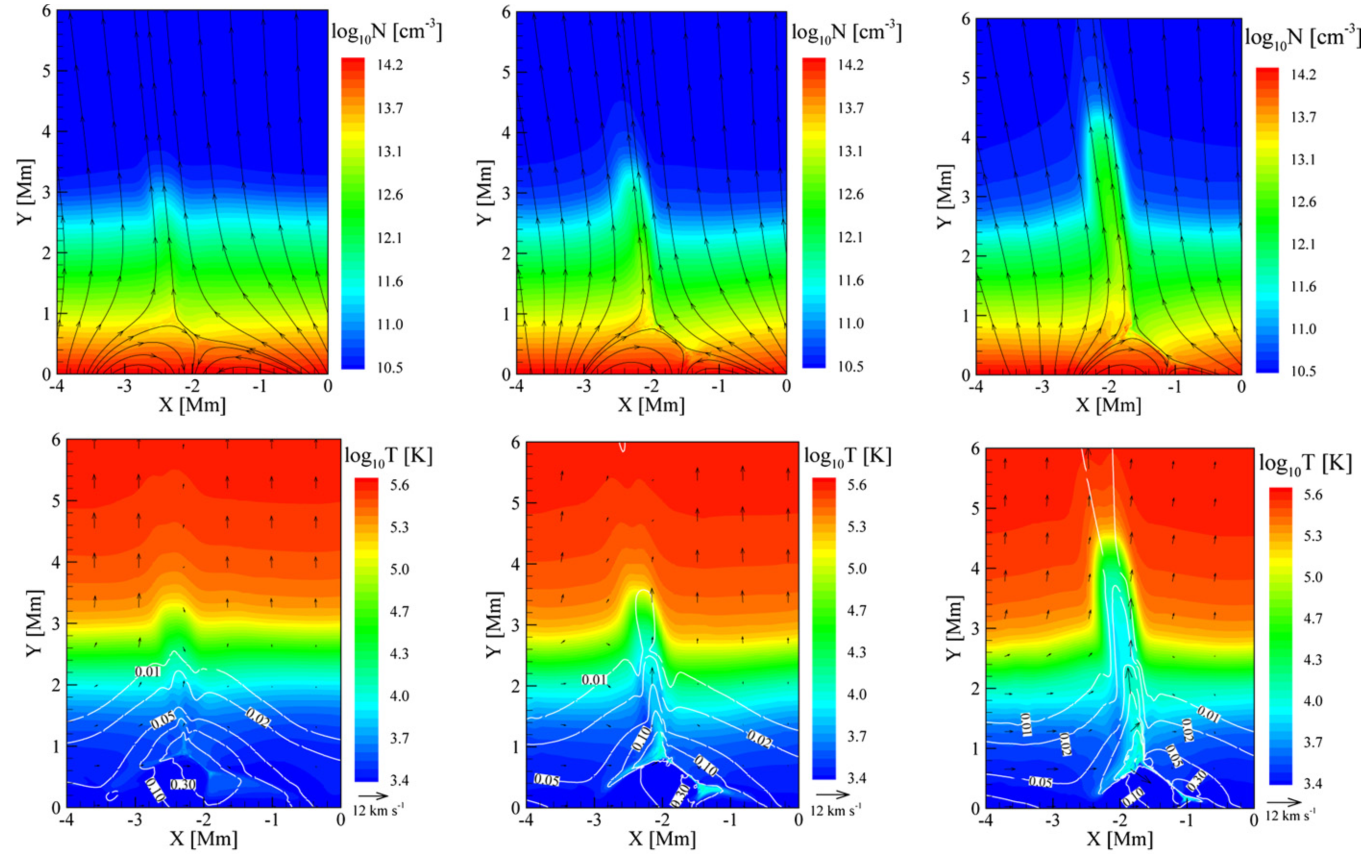

(a) $t = 1.0$ minute (b) $t = 2.8$ minutes (c) $t = 4.3$ minutes

Figure 2. Calculated distributions of number density N and temperature T at $t = 1.0$ minute, $t = 2.8$ minutes, and $t = 4.3$ minutes, where streamlines in the top row denote magnetic field lines and black arrows and white lines in the bottom row indicate velocity and the values of β, respectively.

(A color version of this figure is available in the online journal.)

The heated plasma is expelled along the current concentration into the outflow region. In contract with the case in the inflow regions, the plasma at high temperature appears both in the diffusion and outflow regions. As the magnetic reconnection proceeds, the part of the heated plasma traveling toward high altitudes along the new flux tube develops into a jet. As the heated plasma flows upward, its temperature decreases a little due to large radiative cooling and the lack of any extra heating. At the same time, the heated regions grow both in the horizontal and the vertical directions. As a result, a cusp or inverted Y-shaped structure develops, as seen in the distributions of number density and temperature at $t = 2.8$ minutes. At that time, the cusp size is about 1.5 Mm and the jets reach about 3.4 Mm. Apart from these hot features, cool plasma is revealed to travel upward on the left side of jet as well, which is associated with the sling-shot effect, as discussed by Yokoyama & Shibata (1995). At $t = 4.3$ minutes, the jet head reaches about 4.5 Mm. Compared with that at $t = 2.8$ minutes, the cusp structure shrinks at the moment. We can also see that the width of the simulated jet is about 350 km and that its average velocity is about 10 km s^{-1}, which is comparable with the characteristic local Alfvén speed around the diffusion region. It should be noted that these simulated jet parameters are in good agreement with typical observations of chromospheric anemone jets.

In Figure 3, zoom-ins around the area by the reconnection region are shown, where the calculated distributions of current density J, temperature T, and number density N at $t = 3.85$ minutes, $t = 4.00$ minutes, and $t = 4.01$ minutes are displayed. In this figure, streamlines stand for magnetic field lines and black arrows denote velocity. It can be seen that as the horizontal advection proceeds, the current sheet becomes thinner and longer. Eventually, the system reaches a configuration where the ratio between the length and width of the current sheet makes it unstable to tearing. As a result, the current sheet breaks up into several parts with plasmoids of different sizes formed in between. Pushed by the reconnection outflow, these plasmoids move both upward and downward with a velocity of about 30 km s^{-1}. During their move, some plasmoids expand, and some interact and merge with other plasmoids. Soon after the plasmoids reach the outflow regions, they collide with the magnetic fields there and are quickly destroyed and disappear (within 0.6 s) due to secondary magnetic reconnection. It is evident that the plasmoids share many commonalities with bright blobs observed in the jets. Both of them are formed in one of the legs of the inverse Y-shaped footpoints and appear manifoldly as well as recurrently in the same location. Along the legs of the inverse Y-shaped footpoints, both of them are ejected bi-directionally. Soon after their formation, both of them lose their shapes, with the upward moving ones merging into jet and the downward ones sinking into the lower atmosphere. Also, both of them exhibit high-temperature and high-density features. These common features indicate that bright blobs observed in the chromospheric anemone jets may be the counterparts of plasmoids produced during magnetic reconnection due to the tearing instability.

Figure 4 shows the calculated distributions of the thermal pressure P and vertical velocity V_y at the same time point

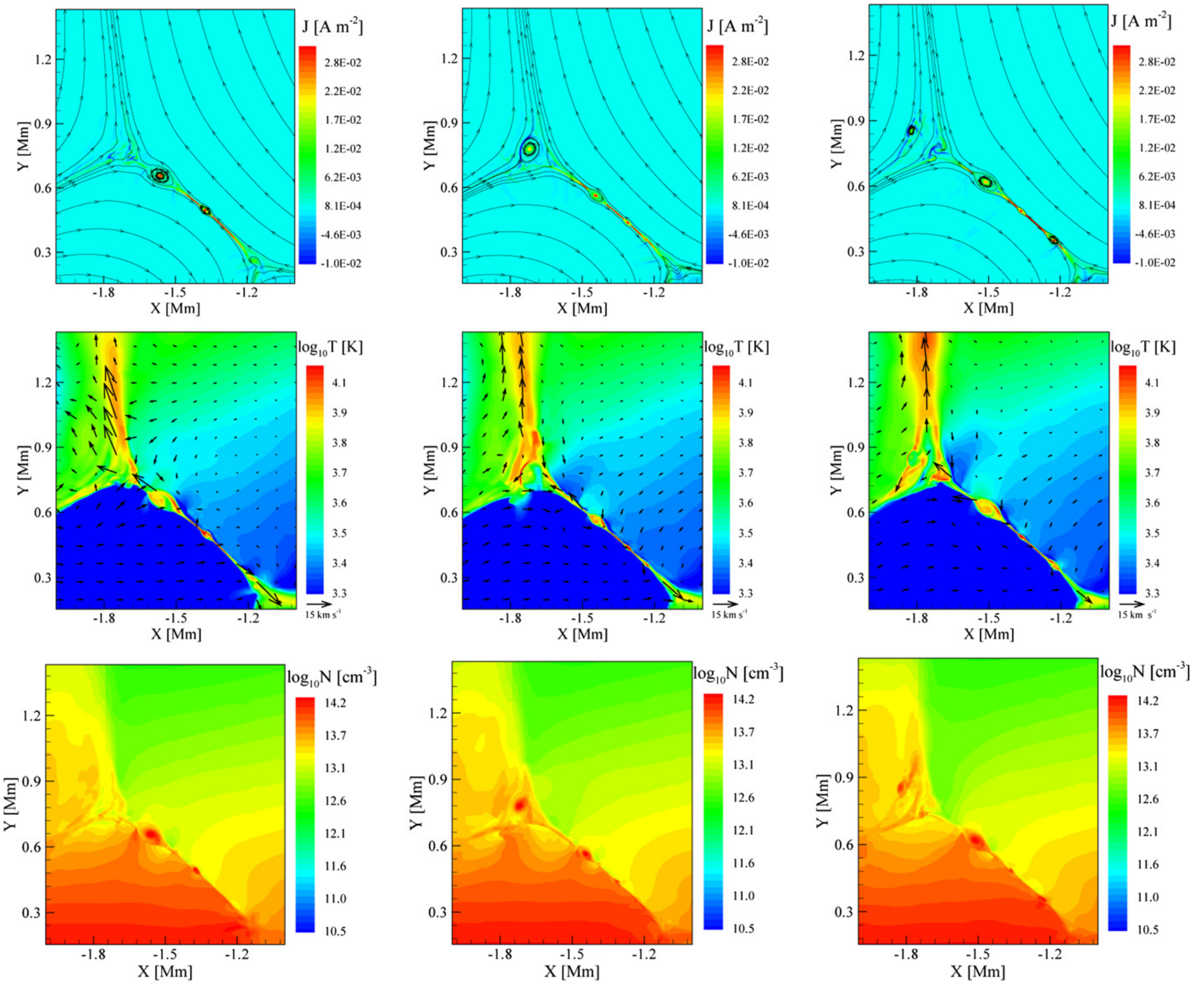

(a) t = 3.85 minutes (b) t = 4.00 minutes (c) t = 4.01 minutes

Figure 3. Calculated distributions of current density *J*, temperature *T*, and number density *N* at $t = 3.85$ minutes, $t = 4.00$ minutes, and $t = 4.01$ minutes, which are zoomed in around the area of the reconnection region. In this figure, streamlines stand for magnetic field lines and black arrows denote velocity.

(A color version of this figure is available in the online journal.)

and in the same region as in Figure 3. From this figure, we can see that at $t = 3.85$ minutes, the big plasmoid, whose thermal pressure is several times larger than the typical value of its surroundings, is ejected quickly upward along the current sheet. At $t = 4.00$ minutes, it enters the outflow region and starts to reconnect with the magnetic fields there. Also, the thermal pressure P increases greatly there. It is surprising, only after about 0.6 s, i.e., at $t = 4.01$ minutes, the plasmoid almost disappears as shown in the current density plot in Figure 3. Naturally, the quick disappearance of the plasmoid leads to the quick release of its high-pressure plasma. As a result, a sudden increase in the thermal pressure occurs in the outflow region, which produces the high-velocity impulse observed around $x = -1.7$ Mm and $y = 1.3$ Mm. The high-velocity impulse moves at a fast speed traveling out of the region after 6 s. Meantime, another plasmoid comes to the outflow region and the process discussed above repeats itself.

3.2. Outwardly Propagating Velocity Pulses

Figure 5 shows the calculated distribution of vertical velocity V_y at $t = 4.3$ minutes in the full domain, where streamlines denote magnetic field lines. In this figure, AMR blocks of different refinement levels are overlaid as white squares. Each block has 12×12 cells. During the computation, five levels of grid refinement are used to identify the current sheet region. From this figure, we can see that the blocks of higher refinement levels automatically cluster near the dynamically evolved current sheet region, across which there are about 20 grid points with a grid spacing of about 1.25 km. On the other hand, a grid cell size of about 20 km is arranged in other regions, as shown in Figure 5.

Combining the velocity distribution with the number density and temperature as shown in Figure 2, we can see a chain of high-velocity impulses propagate upward along the jet, which is launched from the outflow region. Eventually, the pulses reach the solar corona and continually propagate upward until they

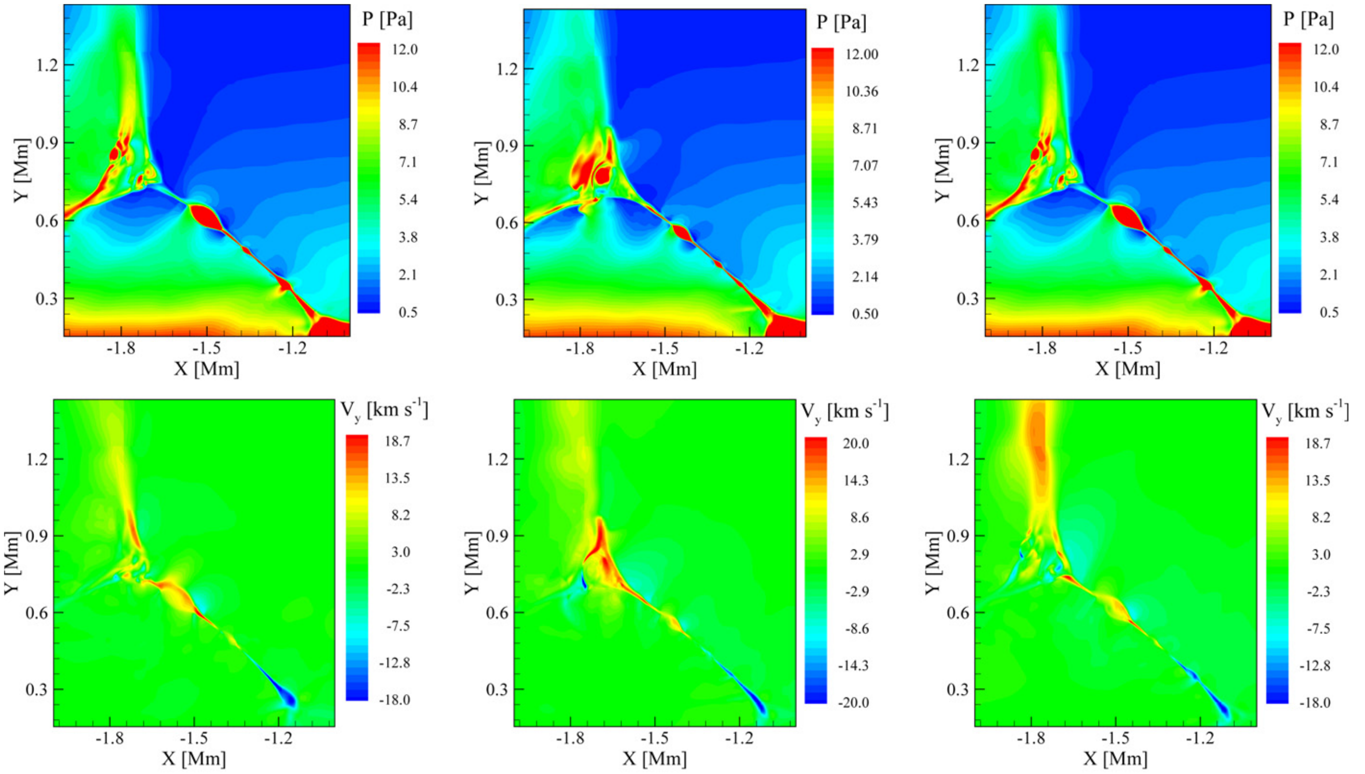

(a) t = 3.85 minutes (b) t = 4.00 minutes (c) t = 4.01 minutes

Figure 4. Calculated distributions of thermal pressure P and vertical velocity V_y at the same time and in the same region as in Figure 3.

(A color version of this figure is available in the online journal.)

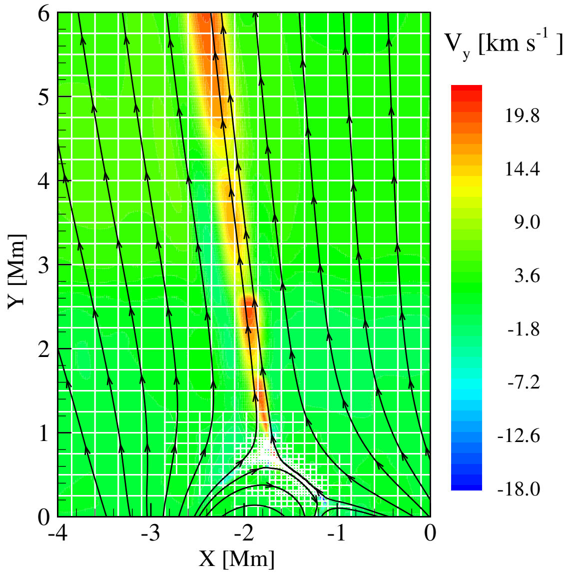

Figure 5. Calculated distributions of vertical velocity V_y at $t = 4.3$ minutes, where streamlines denote magnetic field lines and white squares are AMR blocks of different refinements. In every block, there are 12×12 cells.

(A color version of this figure is available in the online journal.)

leave the computational domain. We can also see that even though the high-velocity impulses go through the transition region and into the solar corona, their amplitudes are not so large as to put them into the upper chromosphere.

To investigate the nature of the high-velocity impulses, Figure 6 shows the profiles of number density N, thermal pressure P, vertical velocity V_y, and temperature T along the reconnected flux tube at $t = 4.3$ minutes. Figure 7 also shows the time variation of these profiles between 4.40 minutes and 4.53 minutes, zoomed into 1–3 Mm with a time step of 0.77 s.

Both Figures 6 and 7 show that across the front of a high-velocity structure, there is a sharp jump for number density, thermal pressure, temperature, and velocity. From Figure 7, we can see that when the jump of the high-velocity structure is at a height of about 2.6 Mm, its propagation speed is about 40 km s^{-1}. Compared with the local sound speed of about 10 km s^{-1}, the high-velocity structures propagate upward at supersonic speeds. The propagation velocity of the high-velocity structures and the velocity amplitude at their front basically satisfy the local Rankine–Hugoniot relation (Suematsu et al. 1982; Shibata & Suematsu 1982), which indicates that the high-velocity impulse is essentially a slow-mode shock propagating in the jet. We could roughly estimate the energy flux of the slow-mode shock as $E_{\rm shock} = 0.5\rho v^3 - 0.5\rho_{\rm flow} v_{\rm flow}^3$, where ρ and v denote the total density and the velocity of the plasma, respectively; $\rho_{\rm flow}$ and $v_{\rm flow}$ are the density and velocity of the background flow, respectively. Taking the shock displayed in Figure 7 as an example, when the shock arrives at the height of about 2.6 Mm, the total density and velocity there are about 4.46×10^{-9} kg m^{-3} and 20 km s^{-1}, respectively. On the other hand, before the shock arrives at this height, we could obtain that the density and velocity of the flow are about 3.55×10^{-9} kg m^{-3} and 10 km s^{-1}, respectively. So, the energy flux of the slow-mode shock is about 26.8 W m^{-2}, which is higher than that of the flow (about 17.8 W m^{-2}).

Figure 8 shows the long-duration (from $t = 2$ minutes to $t = 6$ minutes) profiles of vertical velocity V_y and number density N along the same reconnected flux tube as in Figure 6 with a time increment of 1.54 s. We can see that there is a chain of slow-mode

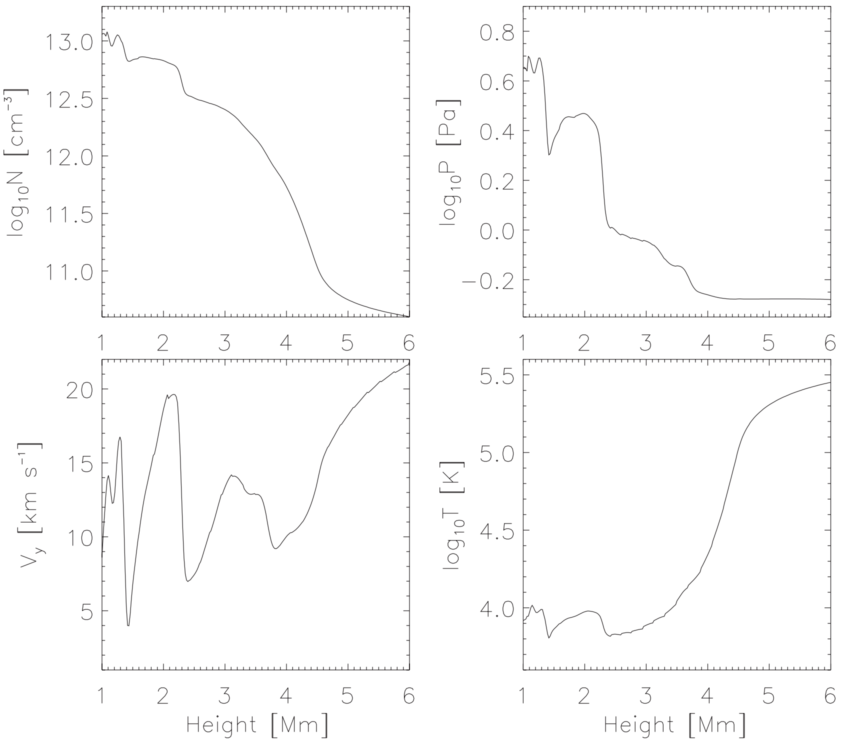

Figure 6. Calculated profiles of number density N, thermal pressure P, vertical velocity V_y, and temperature T along the reconnected flux tube in the jet at $t = 4.3$ minutes.

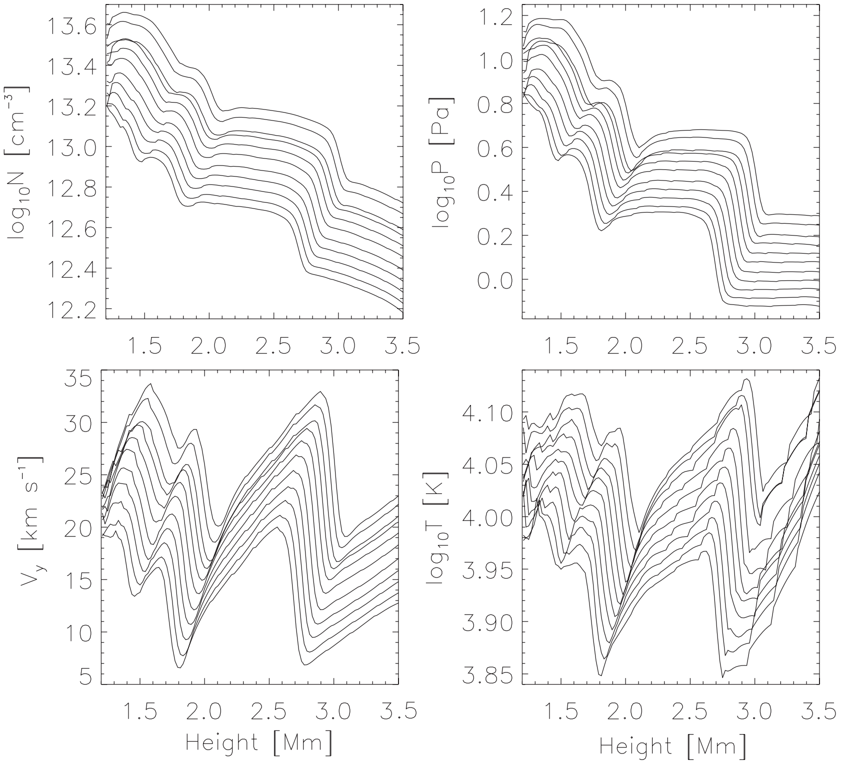

Figure 7. Calculated profiles of number density N, thermal pressure P, vertical velocity V_y, and temperature T along the same reconnected flux tube as in Figure 6 but from 1 Mm to 3 Mm and from $t = 4.40$ minutes to $t = 4.53$ minutes, where each curve shows the profile every 0.77 s.

shocks propagating upward from the footpoint of the jet. As they pass the chromosphere, the slow-mode shocks get stronger and faster. However, when going through the transition region into the corona, they are partially dissipated as a result of the high thermal conduction there. As is known, collisions between the shock and the transition region will lift up the transition region, therefore ejecting material of the chromosphere that forms spicules or surges (Suematsu et al. 1982; Shibata & Suematsu 1982; Kudoh & Shibata 1999; Hansteen et al. 2006; Matsumoto & Shibata 2010). However, from the profiles of

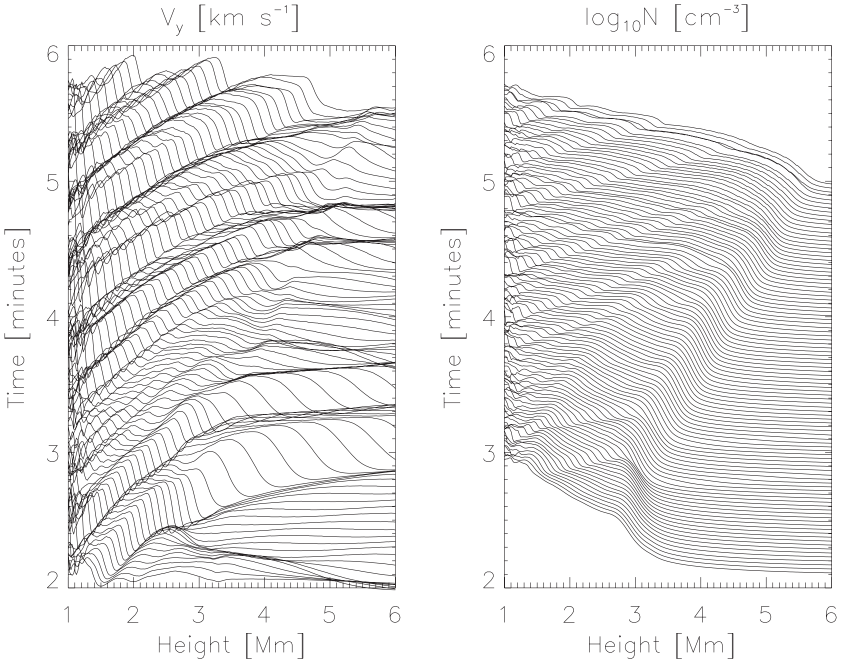

Figure 8. Calculated profiles of vertical velocity and number density N along the same reconnected flux tube as in Figure 6 but from $t = 2$ minutes to $t = 6$ minutes, where profiles at various times are stacked with a uniform increment of 1.54 s.

number density N, we do not see evidence for the lifting-up and associated falling-down of the transition region with the passage of the shocks. The reasons may be as follows. First, the shocks generated here are not very strong, with average Mach numbers of only about 3. Second, the shocks dissipate due to thermal conduction as they arrive at the transition region and run into the corona. So, the jet produced here may be mainly driven by the magnetic reconnection, while being only slightly influenced by the passage of the shock waves.

4. SUMMARY AND DISCUSSION

In this article, a 2.5D MHD model is used to simulate chromospheric anemone jets associated with MMFs. A realistic energy equation, which includes radiation losses, thermal conduction, and coronal heating, is considered. A horizontal component of velocity is prescribed at the bottom of the computational domain to describe the motion of MMFs. With this MHD model, we simulate the reconnection between MMFs and pre-existing ambient fields as a result of the collision between them.

The jet produced in the simulation is consistent with typical observations of chromospheric anemone jets. Carried by the horizontal flow, the MMFs migrate toward the pre-existing ambient field region. Then, the interface separating them deforms to generate a current sheet. When the current density is sufficiently enhanced, reconnection between the MMFs and the pre-existing ambient fields becomes prominent. As a result, the plasma in the diffusion region is heated up by the released magnetic energy and the heated plasma is ejected both upward and downward along the current concentration into the outflow region. As the magnetic reconnection proceeds, the upward heated plasma gradually develops into a jet. At the same time, the heating region enlarges both in the horizontal and vertical directions to form a cusp or inverted Y-shaped structure, where the cusp size is about 1.5 Mm. From the simulation results, we recover a jet width of about 350 km and an average velocity of about 10 km s^{-1}. It should be noted that the simulation also produced cool plasma going upward as a result of the sling-shot effect.

The plasmoids that are generated during magnetic reconnection as a result of the tearing instability share many features with the bright blobs observed in the chromospheric anemone jets. As reconnection occurs, the ratio between the length and width of the current sheet makes it unstable to tearing. Then, the current sheet breaks up into several parts and many plasmoids of different sizes form. Like bright blobs observed in the jets, plasmoids move both upward and downward with some becoming larger and some merging with others. Once the plasmoids reach the outflow regions, they collide with the magnetic fields there and are quickly destroyed, disappearing through reconnection. It is evident that both plasmoids and bright blobs are formed in one of the legs of the inverse Y-shaped footpoints and appear manifoldly as well as recurrently at the same location. Along the legs of the inverse Y-shaped footpoints, both of them are ejected and quickly lose their shapes, with the upward moving ones merging into the jet and the downward moving ones sinking into the lower atmosphere. Most importantly, both of them exhibit high-temperature and high-density features and have similar velocities of about 30 km s^{-1}.

The simulated results further show that a sudden increase in the thermal pressure at the footpoint of the jet, due to the collisions of impacting plasmoids, produces slow-mode shocks propagating in the jet. When a plasmoid is ejected upward, it quickly enters the outflow region. This results in fast reconnection with the pre-existing magnetic fields, which causes a fast release of the high-pressure plasma originally stored in the plasmoid. As a result, the thermal pressure increases substantially, which induces a slow-mode shock. Launched from the footpoint of the jet, the chain of slow-mode shocks propagates upward along the jet at an average velocity of about 30 km s^{-1}. When the shocks pass through the transition region and reach the corona, they experience some dissipation as a result of high thermal conduction. Also, they do not show evidence for lifting-up of the transition region, as was seen in previous works, which indicates that the jet generated in our simulation mainly consists of matter ejected by magnetic reconnection.

Compared with previous studies (e.g., Nishizuka et al. 2008; Matsumoto & Shibata 2010), the treatment of the energetics is improved. The present model has a high Rm number and improved the spatial resolution. This allowed us to self-consistently simulate the chromospheric anemone jets associated MMFs, which we have found to be comparable with the ones observed. Also, a chain of slow-mode shocks propagates in the jet and the jet itself is driven by reconnection, not by the shocks. Since the solar chromosphere is a partially ionized plasma, collisions between electrons, ions, and neutrals could play an important role in reconnection (Singh et al. 2011). We plan on evaluating the influence of ambipolar diffusion and ionization on the dynamic process presented here. Another issue may arise since this work is restricted to a 2.5D model, which is in part based on considerations of computational time and resources, as well as the added complexity of the reconnection process in 3D. Certainly, a loss of one degree of freedom may affect the flows and energetics of the system (Martínez-Sykora et al. 2009; Pariat et al. 2009; Moreno-Insertis & Galsgaard 2013), such as the loss of flow along the guide field as noted by Jiang et al. (2011) or the overestimating of the coalescence instability, as indicated by Dahlburg & Einaudi (2002). However, restricting this study to 2D provides much better control of the processes at work and allows us to concentrate on the process we want to study, namely, the formation of the jet in response to the coalescent motion of the footpoint of the magnetic field lines. In future, we also plan to extend this work to a fully 3D simulation and check the impact of the third dimension on the dynamics presented here.

L.P. thanks E. Marsch, H. Tian, P.-F. Chen, and J. Zhang for helpful discussions. This work at Peking University is supported by the NSFC under contract Nos. 41174148, 40890162, 41222032, and 40931055. L.P. is also supported by the NSFC under contract Nos. 41031066, 41204127, 41204105, as well as the China Postdoctoral Science Foundation under contract No. 452101480342. H.P. gratefully acknowledges kind hospitality at Peking University. The numerical calculations have been completed on the SIGMA Cluster computing system of the State Key Laboratory for Space Weather.

REFERENCES

Abbett, W. P. 2007, ApJ, 665, 1469
Aiouaz, T., Peter, H., & Keppens, R. 2005, A&A, 442, L35
Brooks, D. H., Kurokawa, H., & Berger, T. E. 2007, ApJ, 656, 1197
Cirtain, J. W., Golub, L., Lundquist, L., et al. 2007, Sci, 318, 1580
Cook, J. W., Cheng, C.-C., Jacobs, V. L., & Antiochos, S. K. 1989, ApJ, 338, 1176
Dahlburg, R., & Einaudi, G. 2002, PhLA, 294, 101
Feng, X., Zhang, S., Xiang, C., et al. 2011, ApJ, 734, 50
Guglielmino, S. L., Zuccarello, F., Romano, P., & Bellot Rubio, L. R. 2008, ApJL, 688, L111
Hackenberg, P., Marsch, E., & Mann, G. 2000, A&A, 360, 1139
Hagenaar, H. J., & Shine, R. A. 2005, ApJ, 635, 659
Hansteen, V. H., De Pontieu, B., Rouppe van der Voort, L., van Noort, M., & Carlsson, M. 2006, ApJL, 647, L73
Hansteen, V. H., & Leer, E. 1995, JGR, 100, 21577
Harvey, K., & Harvey, J. 1973, SoPh, 28, 61
Isobe, H., Proctor, M. R. E., & Weiss, N. O. 2008, ApJL, 679, L57
Jiang, R. L., Shibata, K., Isobe, H., & Fang, C. 2011, ApJL, 726, L16
Katsukawa, Y., Berger, T. E., Ichimoto, K., et al. 2007, Sci, 318, 1594
Kudoh, T., & Shibata, K. 1999, ApJ, 514, 493
Martínez-Sykora, J., Hansteen, V., De Pontieu, B., & Carlsson, M. 2009, ApJ, 701, 1569
Matsumoto, T., & Shibata, K. 2010, ApJ, 710, 1857
Moreno-Insertis, F., & Galsgaard, K. 2013, ApJ, 771, 20
Morita, S., Shibata, K., Ueno, S., et al. 2010, PASJ, 62, 901
Morita, S., Shibata, K., Ueno, S., et al. 2012, in ASP Conf. Ser. 454, Hinode-3: The 3rd Hinode Science Meeting, ed. T. Sekii, T. Watanabe, & T. Sakurai (San Francisco, CA: ASP), 95
Nishizuka, N., Nakamura, T., Kawate, T., Singh, K. A. P., & Shibata, K. 2011, ApJ, 731, 43
Nishizuka, N., Shimizu, M., Nakamura, T., et al. 2008, ApJL, 683, L83
Pariat, E., Antiochos, S. K., & DeVore, C. R. 2009, ApJ, 691, 61
Ravindra, B. 2006, SoPh, 237, 297
Sheeley, N. R., Jr. 1969, SoPh, 9, 347
Shibata, K., Ishido, Y., Acton, L. W., et al. 1992, PASJ, 44, L173
Shibata, K., Nakamura, T., Matsumoto, T., et al. 2007, Sci, 318, 1591
Shibata, K., & Suematsu, Y. 1982, SoPh, 78, 333
Shimojo, M., Shibata, K., & Harvey, K. L. 1998, SoPh, 178, 379
Singh, K. A. P., Isobe, H., Nishizuka, N., Nishida, K., & Shibata, K. 2012, ApJ, 759, 33
Singh, K. A. P., Shibata, K., Nishizuka, N., & Isobe, H. 2011, PhPl, 18, 111210
Suematsu, Y., Shibata, K., Neshikawa, T., & Kitai, R. 1982, SoPh, 75, 99
Yang, L., He, J., Peter, H., et al. 2013, ApJ, 770, 6
Yokoyama, T., & Shibata, K. 1995, Natur, 375, 42
Yokoyama, T., & Shibata, K. 1996, PASJ, 48, 353
Zhang, H., Ai, G., Wang, H., Zirin, H., & Patterson, A. 1992, SoPh, 140, 307
Zhang, S.-H., Feng, X.-S., Wang, Y., & Yang, L.-P. 2011, ChPhL, 28, 089601
Ziegler, U. 2004, JCoPh, 196, 393